nature physics

LETTERS

PUBLISHED ONLINE: 24 OCTOBER 2016 | DOI: 10.1038/NPHYS3928

Interlayer electron–phonon coupling in WSe_2/hBN heterostructures

Chenhao Jin[1†], Jonghwan Kim[1†], Joonki Suh[2], Zhiwen Shi[1], Bin Chen[3], Xi Fan[3], Matthew Kam[1], Kenji Watanabe[4], Takashi Taniguchi[4], Sefaattin Tongay[3], Alex Zettl[1,5,6], Junqiao Wu[2,5] and Feng Wang[1,5,6]*

Engineering layer–layer interactions provides a powerful way to realize novel and designable quantum phenomena in van der Waals heterostructures[1–16]. Interlayer electron–electron interactions, for example, have enabled fascinating physics that is difficult to achieve in a single material, such as the Hofstadter's butterfly in graphene/boron nitride (hBN) heterostructures[5–10]. In addition to electron–electron interactions, interlayer electron–phonon interactions allow for further control of the physical properties of van der Waals heterostructures. Here we report an interlayer electron–phonon interaction in WSe_2/hBN heterostructures, where optically silent hBN phonons emerge in Raman spectra with strong intensities through resonant coupling to WSe_2 electronic transitions. Excitation spectroscopy reveals the double-resonance nature of such enhancement, and identifies the two resonant states to be the A exciton transition of monolayer WSe_2 and a new hybrid state present only in WSe_2/hBN heterostructures. The observation of an interlayer electron–phonon interaction could open up new ways to engineer electrons and phonons for device applications.

Van der Waals heterostructures of atomically thin two-dimensional (2D) crystals are a new class of material in which novel quantum phenomena can emerge from layer–layer interactions[1–16]. For example, electron–electron interactions between adjacent 2D layers can give rise to a variety of fascinating physical behaviours: the interlayer moiré potential between the graphene and hBN layers leads to mini-Dirac cones and the Hofstadter's butterfly pattern in graphene/hBN heterostructures[5–10]; electronic couplings between MoS_2 and MoS_2 layers lead to a direct- to indirect-bandgap transition in bilayer MoS_2 (refs 11,12); and Coulomb interactions between $MoSe_2$ and WSe_2 layers lead to interlayer exciton states in $MoSe_2/WSe_2$ heterostructures[13,14]. Similar to electron–electron interactions, electron–phonon interactions also play a key role in a wide range of phenomena in condensed matter physics: the electron–phonon coupling sets the intrinsic limit of electron mobility[17], dominates the ultrafast carrier dynamics[18], leads to the Peierls instability[19], and enables the formation of Cooper pairs[20]. Exploiting interactions between electrons in one layered material and phonons in an adjacent material could enable new ways to control electron–phonon coupling and realize novel quantum behaviour that has not previously been possible. For example, it has been recently shown that electrons in monolayer FeSe can couple strongly with phonons in the adjacent $SrTiO_3$ substrate, which may play an important role in the anomalously high critical temperature for superconductivity in the system[21,22]. However, the unusual interlayer electron–phonon interactions in the van der Waals heterostructures have been little explored so far, although there have been indications that interlayer interactions between graphene electrons and the substrate phonons is a limiting factor for higher graphene electron mobility at room temperature[23,24].

Here we report, for the first time, an extraordinary interlayer electron–phonon coupling in WSe_2/hBN heterostructures, as illustrated in Fig. 1a. The vibration modes of the hBN lattice (labelled with red arrows) can significantly modulate the behaviour of electrons and holes in WSe_2 (red and blue clouds), thus enabling efficient interlayer electron–phonon coupling. Experimentally, such interaction manifests as emerging resonant Raman scattering processes that involve both hBN phonon vibrations and WSe_2 electronic resonances: two prominent new Raman peaks appear in the heterostructure composed of WSe_2 encapsulated in hBN flakes, with the Raman shifts corresponding to the hBN ZO phonon mode and the hBN ZO + WSe_2 A_{1g} combinatorial mode, respectively. These Raman modes are remarkably strong, with intensities three orders of magnitude higher than the Raman signal of phonons in pure hBN. Excitation spectroscopy reveals that the new Raman peaks of hBN ZO phonons are enhanced by WSe_2 electronic transitions in a double-resonance process. This double resonance involves both the well-known A exciton of monolayer WSe_2, and a rather surprising new electronic transition present only in the WSe_2/hBN heterostructures that originates from the interactions between the adjacent WSe_2 and hBN layers. In addition, we show that the new Raman peaks from the interlayer electron–phonon couplings in the heterostructure can be controlled efficiently through electrostatic gating of the monolayer WSe_2. Our study demonstrates the presence of interlayer electron–phonon interactions in van der Waals heterostructures, which will be important for understanding electron behaviour from carrier mobility to energy relaxation dynamics in 2D materials, and offers new opportunities to engineer novel quantum phenomena in van der Waals heterostructures.

Figure 1b shows an optical microscope image of the heterostructure, where monolayer WSe_2 is encapsulated with thin hBN flakes (∼10 nm thick) by a dry transfer method using a polyethylene terephthalate (PET) stamp (see Methods). The contact electrodes are fabricated on the exposed part of WSe_2 outside the top hBN layer, as illustrated in Fig. 1c, which allows us to study the doping-dependent behaviour. Figure 2a shows light emission

[1]Department of Physics, University of California at Berkeley, Berkeley, California 94720, USA. [2]Department of Materials Science and Engineering, University of California at Berkeley, Berkeley, California 94720, USA. [3]School for Engineering of Matter, Transport and Energy, Arizona State University, Tempe, Arizona 85287, USA. [4]National Institute for Materials Science, 1-1 Namiki, Tsukuba 305-0044, Japan. [5]Material Science Division, Lawrence Berkeley National Laboratory, Berkeley, California 94720, USA. [6]Kavli Energy NanoSciences Institute at University of California Berkeley and Lawrence Berkeley National Laboratory, Berkeley, California 94720, USA. †These authors contributed equally to this work. *e-mail: fengwang76@berkeley.edu

© 2016 Macmillan Publishers Limited, part of Springer Nature. All rights reserved.

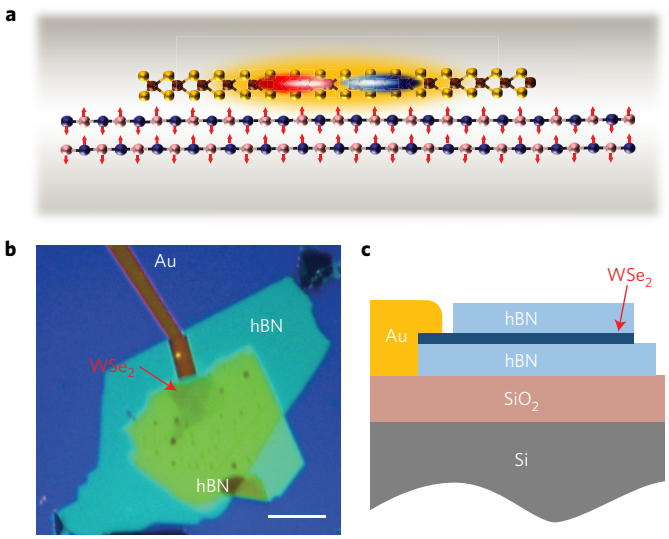

Figure 1 | WSe_2/hBN heterostructures. a, Illustration of interlayer electron–phonon coupling. Red arrows in hBN (bottom) and red/blue clouds in WSe_2 (top) show schematically the phonon vibration in hBN and the electron/hole states in WSe_2, respectively. Such interlayer electron–phonon interactions can lead to novel electronic and optical properties in the van der Waals heterostructure. **b**, Optical microscope image of WSe_2 encapsulated in hBN layers. The scale bar corresponds to 5 μm. **c**, Illustration of the gate-tunable device. A contact electrode (Au/Ti) is fabricated on the exposed part of WSe_2 outside the top hBN layer to allow for electrostatic gating.

spectra of the heterostructure with different photoexcitation energies (E_{exc} = 1.849, 1.857 and 1.862 eV) at 77 K. The prominent peaks at 1.71 eV and 1.68 eV are the well-known exciton and trion photoluminescence (PL) in pristine WSe_2 (ref. 25). Surprisingly, we observe two additional strong peaks that do not exist in the emission spectra of either pristine WSe_2 or hBN, as labelled by the green and orange arrows. These unique emission peaks in the heterostructures are fairly unusual in several aspects. Most notably, their peak energies shift by exactly the same amount as the excitation light, a defining signature of Raman scattering processes. In addition, these new Raman peaks show a distinct polarization dependence: the Raman intensities are strongest for parallel incident and outgoing photon polarizations (red curves), and disappear completely in the cross-polarization configuration (black curves). In contrast, WSe_2 exciton and trion PL intensities show negligible linear polarization dependence in these exfoliated WSe_2 encapsulated in hBN. Such a distinctive polarization dependence allows us to obtain clean Raman features without the PL background simply by subtracting the cross-polarization spectra from the parallel-polarization spectra. The black curve in Fig. 2b shows the subtracted spectrum for photoexcitation at 1.849 eV. Two prominent Raman peaks with sharp edges located at 820 (mode I) and 1,070 cm^{-1} (mode II) are clearly observed.

Raman modes with energy shifts at 820 (mode I) and 1,070 cm^{-1} (mode II) do not exist in either isolated WSe_2 or hBN. The Raman-allowed hBN phonon mode is the E_{2g} mode at 1,367 cm^{-1} (refs 26,27). On the other hand, both the A_{1g} and E_{2g} Raman modes of WSe_2 are located at around 250 cm^{-1} (ref. 28). Instead, the Raman peak energies in WSe_2/hBN heterostructures match well with the hBN ZO mode (820 cm^{-1}) and hBN ZO + WSe_2 A_{1g} mode (820 cm^{-1} + 250 cm^{-1}) (refs 26,27). Consequently, we attribute the new Raman modes to the hBN ZO phonon and the combinatorial hBN ZO and WSe_2 A_{1g} phonon in WSe_2/hBN heterostructures. These new Raman peaks of the heterostructures exhibit several surprising properties. First, the hBN ZO mode (see inset of Fig. 2b) is not Raman active, and thus is completely absent in the Raman measurement of pristine hBN[27]. The red curve in Fig. 2b is a Raman spectrum from pristine hBN (measured on the same heterostructure but outside WSe_2), where the only observable hBN Raman peak is the in-plane E_{2g} mode at 1,367 cm^{-1} (the broad peak at 950 cm^{-1} corresponds to the second-order Raman mode of the Si substrate). Second, and more surprisingly, the observed hBN ZO Raman peak is extraordinary strong: the hBN ZO Raman peak at a photoexcitation of 1.849 eV is more than three orders of magnitude stronger than the hBN E_{2g} mode measured at the same experimental condition (Fig. 2b).

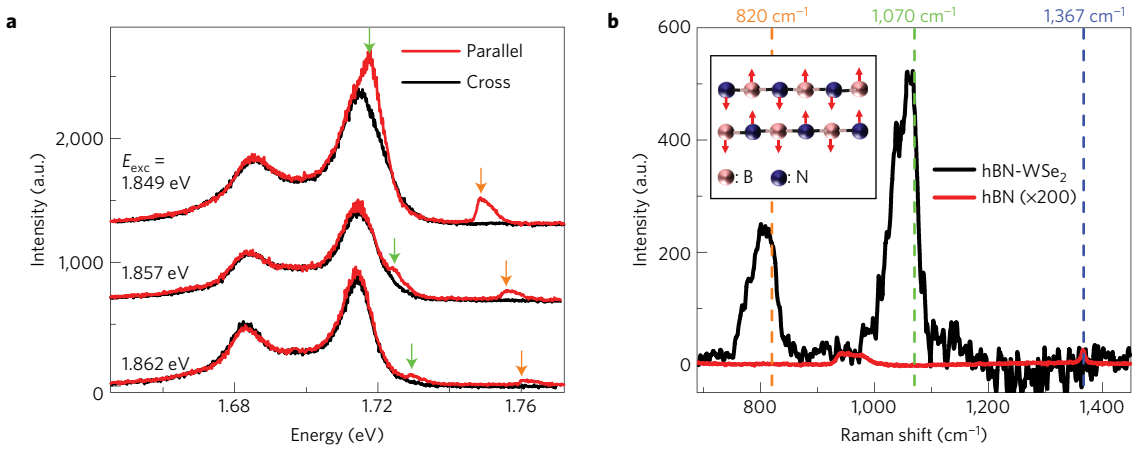

Figure 2 | Emission spectra of a WSe_2/hBN heterostructure at 77 K. a, Light emission spectra of the heterostructure with photoexcitation energies at 1.849, 1.857 and 1.862 eV. In addition to PL from the exciton and trion states in pristine WSe_2 at 1.71 eV and 1.68 eV, two extra Raman peaks (green and orange arrows) are observed, whose peak positions shift linearly with the excitation laser energy. Red and black curves are spectra for parallel and perpendicular excitation and emission polarizations, respectively. Both Raman peaks show a strong polarization dependence and completely disappear in the cross-polarization configuration. **b**, Raman spectrum of the heterostructure with 1.849 eV laser excitation (black curve). Two asymmetric Raman peaks are observed with sharp edges located at 820 and 1,070 cm^{-1} (orange and green dashed lines), corresponding to the hBN ZO mode (820 cm^{-1}) and the hBN ZO + WSe_2 A_{1g} mode (820 cm^{-1} + 250 cm^{-1}), respectively. In contrast, the Raman spectrum of a pure hBN flake with 1.849 eV laser excitation (red curve) shows only one peak at 1,367 cm^{-1} (blue dashed line), which is over three orders of magnitude weaker than the emerging Raman peaks in the heterostructures. Inset illustrates atomic vibrations of the hBN ZO mode.

© 2016 Macmillan Publishers Limited, part of Springer Nature. All rights reserved.

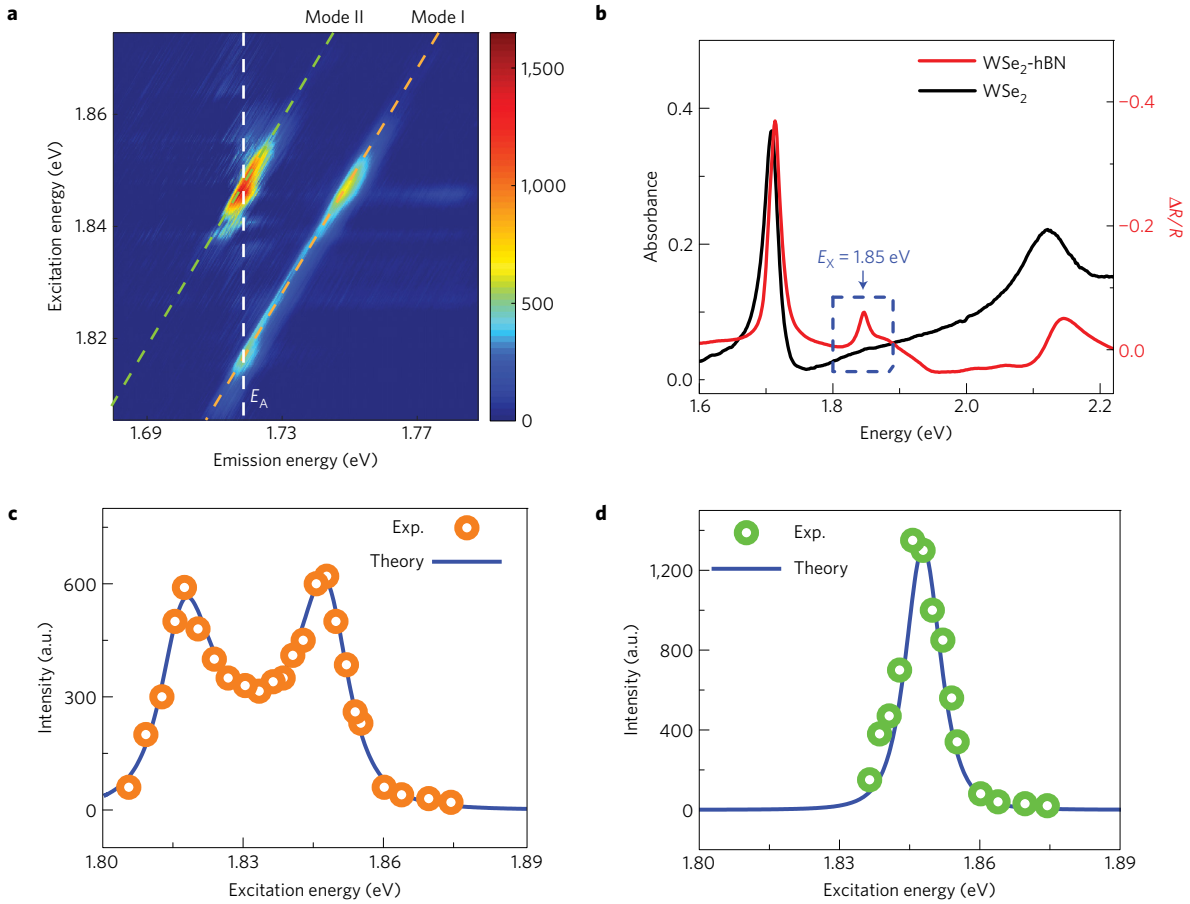

Figure 3 | Resonant Raman process in WSe_2/hBN heterostructures. a, Raman excitation spectroscopy of the heterostructure at 77 K. Horizontal axis, vertical axis and colour scale correspond to emission energy, excitation energy and Raman intensity, respectively. Orange and green dashed lines show the linear dependence between excitation and emission energies for both Raman modes. The Raman intensities of both modes are strongly enhanced when the emission energy matches the WSe_2 A exciton energy at $E_A = 1.71$ eV (white dashed line). On the other hand, mode I also shows enhancement with an excitation energy at 1.85 eV, which does not match with a known optical resonance in pristine WSe_2. **b**, Reflection spectroscopy of heterostructures (red) and pristine WSe_2 (black) at 77 K. Both spectra show prominent optical resonances at 1.71 and 2.12 eV, corresponding to the A and B exciton transitions in WSe_2, respectively. However, a new optical resonance emerges in the heterostructure at $E_X = 1.85$ eV (blue arrow) due to interlayer interaction, which matches exactly with the resonance energy observed in the Raman spectra. **c**,**d**, Resonant Raman profile of mode I (**c**) and mode II (**d**). Blue curves are the theoretically predicted Raman intensity dependence on excitation energy from a double-resonance model. The excellent agreement with experimental results (orange and green circles) confirms that the resonant Raman process is dominated by the double-resonance channel involving both the X peak and the A exciton transition.

To understand the extraordinarily strong Raman peak from the hBN ZO phonon, we perform systematic Raman spectroscopy with photoexcitation energies varying from 1.8 to 1.89 eV. Figure 3a shows a 2D colour plot of the observed Raman spectra, where horizontal axis, vertical axis and colour scale correspond to emission energy, excitation energy and Raman intensity, respectively. Orange and green dashed lines show that the emission and excitation energies have a strictly linear dependence for both modes I and II, confirming that the emission features correspond to Raman peaks. In addition, we observe that the Raman intensities change dramatically with the excitation laser energy. Specifically, mode I shows strong enhancement with an excitation energy at 1.85 eV and 1.82 eV, and mode II shows strong enhancement with an excitation energy at 1.85 eV. Such a sensitive dependence of Raman intensities on photoexcitation energy is a defining feature of resonant Raman processes, where the Raman signal becomes strongly enhanced when the incident or outgoing photons are in resonance with electronic transitions. However, the electronic resonances from hBN are at ultraviolet frequencies due to the large bandgap of hBN (at ∼5.8 eV)[29], and they cannot contribute to the resonant Raman scattering observed in this study. Therefore, the electronic resonances observed in the Raman spectra must originate from WSe_2. Indeed, part of the resonant Raman features matches well with the known exciton resonance in WSe_2: both mode I and mode II show Raman enhancement when the outgoing photon energies match with the A exciton transition in WSe_2 at 1.71 eV (white dashed line in Fig. 3a).

The emerging Raman modes I and II in WSe_2/hBN heterostructures are therefore fairly unique: the phonon excitation is dominated by hBN vibrations, but the electronic excitation is through the neighbouring layer of WSe_2. These peculiar Raman modes thus demonstrate extraordinary interlayer couplings between electronic states in WSe_2 and vibrational modes in hBN (that is, interlayer electron–phonon coupling between van der Waals layers) that have not previously been reported. This interlayer electron–phonon coupling also explains the emergence of hBN ZO phonons in the Raman spectra: the WSe_2/hBN interface has a symmetry different from that of the bulk hBN, and the Raman-forbidden hBN ZO phonon becomes allowed at the interface. In addition, the ZO phonons correspond to out-of-plane vibrations in hBN, which couple more strongly to the atoms in WSe_2 compared to the in-plane E_{2g} phonons in hBN. Further examination of

© 2016 Macmillan Publishers Limited, part of Springer Nature. All rights reserved.

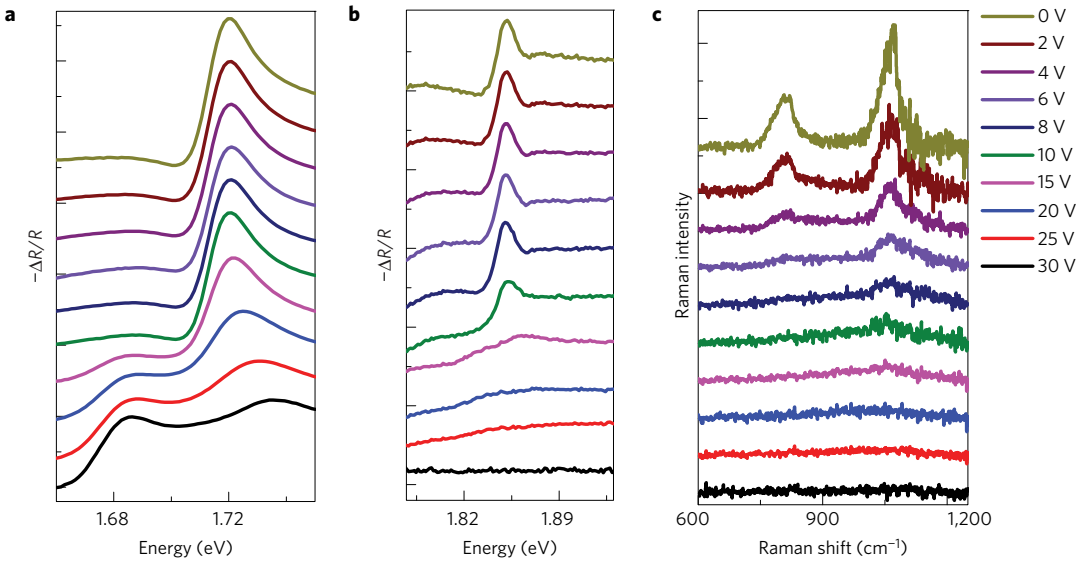

Figure 4 | Varying the interlayer electron–phonon coupling with electrostatic doping. Evolution of the exciton and trion peaks in the reflection spectra (**a**), the X peak resonance in the reflection spectra (**b**), and the resonant hBN Raman peak (**c**) as a function of the gate voltage at 77 K. As the gate voltage changes from 0 V to 30 V, WSe_2 becomes electron doped, and the trion absorption around 1.68 eV becomes more obvious (**a**). At the same time, the X peak (**b**) and resonant hBN Raman peak (**c**) become weaker and disappear completely at a relatively low doping level.

the ZO phonon symmetry shows that the Raman signals should exhibit a perfect linear polarization dependence, as observed in our experiment (Supplementary Information 1).

The strong enhancement of Raman mode I at 1.85 eV excitation energy (Fig. 3a), however, cannot be explained by any known resonances in pristine WSe_2, because neither the incident photon energy (1.85 eV) nor the outgoing photon energy (1.75 eV) matches with the A or B exciton transitions in WSe_2. It suggests that new optical resonances may have been created in WSe_2 due to interactions with the adjacent hBN layers. To investigate this possibility, we performed optical reflection spectroscopy of hBN-encapsulated WSe_2. Indeed, the WSe_2-hBN heterostructure (red curve in Fig. 3b) shows distinctively different reflectance contrast spectra from the pristine one (black curve in Fig. 3b): an additional pronounced optical resonance emerges at 1.85 eV (labelled as the X peak, see blue arrow in Fig. 3b), which matches exactly with the resonance energy observed in the Raman spectra. The emergence of the X peak is further confirmed by photoluminescence excitation (PLE) spectroscopy of the heterostructure (Supplementary Information 2). The other prominent peaks at 1.71 and 2.12 eV are present in both pristine WSe_2 and WSe_2/hBN heterostructures, and they correspond to the well-known A and B exciton transitions of WSe_2, respectively.

Quantitative analysis of Raman excitation spectroscopy provides more detailed information on the interlayer coupling between hBN phonon and WSe_2 electronic states. Orange and green circles in Fig. 3c and d show the dependence of Raman intensity on the excitation energy for modes I and II, respectively. As discussed before, two optical resonances (A exciton and X peak states in WSe_2) are involved in the resonant Raman process, and the double-resonance model yields an energy-dependent Raman intensity in the form of

$$I_{XA}{}^{\alpha}(E) \sim \left| \frac{A_{XA}^{\alpha}}{\left(E_X - E - i\gamma_1\right)\left(E_A + E_{ph}^{\alpha} - E - i\gamma_2\right)} \right|^2 \qquad (1)$$

where $E_A = 1.71$ eV and $E_X = 1.85$ eV are the two resonance energies, γ_1 and $\gamma_2 \sim 7$ meV are the energy broadenings of the resonances, and $\alpha = \mathrm{I}, \mathrm{II}$ labels the two Raman modes, with phonon energies $E_{ph}^{I} = 820\ \mathrm{cm}^{-1}$ and $E_{ph}^{II} = 1{,}070\ \mathrm{cm}^{-1}$. A_{XA}^{α} are constant fitting parameters, and the values are related to the electronic transition oscillator strengths and the electron–phonon coupling matrix elements[30]. The Raman excitation spectral profiles of both modes can be reproduced well by equation (1), shown as blue curves in Fig. 3c,d. For mode I (Fig. 3c), two peaks at 1.847 and 1.818 eV in the Raman excitation spectra correspond to the resonance of the incident photon to the X peak and the outgoing photon to the A peak, respectively. For mode II (Fig. 3d), only one peak appears at 1.848 eV, because the resonances for incident and outgoing photon are close in energy. The excellent agreement between the theory and data confirms that the resonant Raman process is dominated by the double-resonance channel where both the X peak transition and the A exciton transition are important.

In addition, we find that the unique interlayer coupling between WSe_2 and hBN can be controlled effectively through electrostatic gating of WSe_2 in the heterostructure. Figure 4a–c shows the gate-dependent exciton and trion absorption, X peak absorption and resonant Raman spectra of WSe_2 encapsulated in hBN, respectively. When WSe_2 is gated from charge neutral ($V_g = 0$ V) to electron doped ($V_g = 30$ V), the exciton absorption decreases and trion absorption emerges gradually. In contrast, both the X peak in absorption (Fig. 4b) and the resonant hBN Raman peak (Fig. 4c) show a much more sensitive doping dependence than the exciton and trion absorption: both features decrease strongly with the electron doping, and completely disappear at a relatively low doping level. As a result, the hBN ZO phonon Raman intensity can be varied by more than two orders with a carrier density increase of less than $4 \times 10^{12}\ \mathrm{cm}^{-2}$ in WSe_2. This strong doping dependence of the X peak and Raman intensity is fairly surprising, and its origin is not clear. One possibility is that the doped electrons can strongly renormalize the interlayer interactions between WSe_2 and hBN through many-body screening effects, and suppress the optical absorption and Raman features associated with the interlayer couplings[10,31].

In-depth theoretical investigations will be required to reveal the detailed microscopic mechanism that leads to the X peak and the interlayer electron–phonon interactions in WSe_2/hBN heterostructures, which is beyond the present study (Supplementary Information 3). Understanding and further control of such interlayer electron–phonon in the van der Waals heterostructure,

© 2016 Macmillan Publishers Limited, part of Springer Nature. All rights reserved.

which in principle should be widely present, will not only advance our fundamental knowledge of this new class of materials, but also enable new ways to dynamically manipulate electrons and phonons for novel device applications.

Methods

Methods, including statements of data availability and any associated accession codes and references, are available in the online version of this paper.

Received 26 May 2016; accepted 16 September 2016; published online 24 October 2016

References

1. Mak, K. F., McGill, K. L., Park, J. & McEuen, P. L. The valley Hall effect in MoS_2 transistors. *Science* **344,** 1489–1492 (2014).
2. Alden, J. S. *et al*. Strain solitons and topological defects in bilayer graphene. *Proc. Natl Acad. Sci. USA* **110,** 11256–11260 (2013).
3. Lee, C. H. *et al*. Atomically thin p–n junctions with van der Waals heterointerfaces. *Nat. Nanotech.* **9,** 676–681 (2014).
4. van der Zande, A. M. *et al*. Tailoring the electronic structure in bilayer molybdenum disulfide via interlayer twist. *Nano Lett.* **14,** 3869–3875 (2014).
5. Yankowitz, M. *et al*. Emergence of superlattice Dirac points in graphene on hexagonal boron nitride. *Nat. Phys.* **8,** 382–386 (2012).
6. Ponomarenko, L. A. *et al*. Cloning of Dirac fermions in graphene superlattices. *Nature* **497,** 594–597 (2013).
7. Dean, C. R. *et al*. Hofstadter's butterfly and the fractal quantum Hall effect in moiré superlattices. *Nature* **497,** 598–602 (2013).
8. Hunt, B. *et al*. Massive Dirac fermions and Hofstadter butterfly in a van der Waals heterostructure. *Science* **340,** 1427–1430 (2013).
9. Yang, W. *et al*. Epitaxial growth of single-domain graphene on hexagonal boron nitride. *Nat. Mater.* **12,** 792–797 (2013).
10. Shi, Z. *et al*. Gate-dependent pseudospin mixing in graphene/boron nitride moiré superlattices. *Nat. Phys.* **10,** 743–747 (2014).
11. Mak, K. F., Lee, C., Hone, J., Shan, J. & Heinz, T. F. Atomically thin MoS_2: a new direct-gap semiconductor. *Phys. Rev. Lett.* **105,** 136805 (2010).
12. Splendiani, A. *et al*. Emerging photoluminescence in monolayer MoS_2. *Nano Lett.* **10,** 1271–1275 (2010).
13. Rivera, P. *et al*. Valley-polarized exciton dynamics in a 2D semiconductor heterostructure. *Science* **351,** 688–691 (2016).
14. Yu, H. Y., Wang, Y., Tong, Q. J., Xu, X. D. & Yao, W. Anomalous light cones and valley optical selection rules of interlayer excitons in twisted heterobilayers. *Phys. Rev. Lett.* **115,** 187002 (2015).
15. Klimchitskaya, G. L., Mohideen, U. & Mostepanenko, V. M. The Casimir force between real materials: experiment and theory. *Rev. Mod. Phys.* **81,** 1827–1885 (2009).
16. Woods, L. M. *et al*. A materials perspective on Casimir and van der Waals interactions. Preprint at http://arxiv.org/abs/1509.03338 (2015).
17. Price, P. J. Two-dimensional electron transport in semiconductor layers. I. Phonon scattering. *Ann. Phys.* **133,** 217–239 (1981).
18. Rossi, F. & Kuhn, T. Theory of ultrafast phenomena in photoexcited semiconductors. *Rev. Mod. Phys.* **74,** 895–950 (2002).
19. Peierls, R. E. *Quantum Theory of Solids* (Oxford Univ. Press, 1955).
20. Bardeen, J., Cooper, L. N. & Schrieffer, J. R. Theory of superconductivity. *Phys. Rev.* **108,** 1175–1204 (1957).
21. Lee, J. J. *et al*. Interfacial mode coupling as the origin of the enhancement of T_c in FeSe films on $SrTiO_3$. *Nature* **515,** 245–248 (2014).
22. Ge, J.-F. *et al*. Superconductivity above 100 K in single-layer FeSe films on doped $SrTiO_3$. *Nat. Mater.* **14,** 285–289 (2015).
23. Chen, J.-H., Jang, C., Xiao, S., Ishigami, M. & Fuhrer, M. S. Intrinsic and extrinsic performance limits of graphene devices on SiO_2. *Nat. Nanotech.* **3,** 206–209 (2008).
24. Farmer, D. B. *et al*. Utilization of a buffered dielectric to achieve high field-effect carrier mobility in graphene transistors. *Nano Lett.* **9,** 4474–4478 (2009).
25. Jones, A. M. *et al*. Optical generation of excitonic valley coherence in monolayer WSe_2. *Nat. Nanotech.* **8,** 634–638 (2013).
26. Geick, R., Perry, C. H. & Rupprecht, G. Normal modes in hexagonal boron nitride. *Phys. Rev.* **146,** 543–547 (1966).
27. Serrano, J. *et al*. Vibrational properties of hexagonal boron nitride: inelastic X-ray scattering and *ab initio* calculations. *Phys. Rev. Lett.* **98,** 095503 (2007).
28. Sahin, H. *et al*. Anomalous Raman spectra and thickness-dependent electronic properties of WSe_2. *Phys. Rev. B* **87,** 165409 (2013).
29. Watanabe, K., Taniguchi, T. & Kanda, H. Direct-bandgap properties and evidence for ultraviolet lasing of hexagonal boron nitride single crystal. *Nat. Mater.* **3,** 404–409 (2004).
30. Cardona, M. *Light Scattering in Solids I* Vol. 8, 85–92 (Springer, 1983).
31. Song, J. C. W., Shytov, A. V. & Levitov, L. S. Electron interactions and gap opening in graphene superlattices. *Phys. Rev. Lett.* **111,** 266801 (2013).

Acknowledgements

We thank S. Kahn for technical suggestions on heterostructure preparation and J. Yuk for fruitful discussions on sample characterization. This work was primarily supported by the Director, Office of Science, Office of Basic Energy Sciences, Materials Sciences and Engineering Division of the US Department of Energy under Contract No. DE-AC02-05-CH11231 (van der Waals heterostructures program, KCWF16), and was supported in part by previous breakthroughs obtained through the Laboratory Directed Research and Development Program of Lawrence Berkeley National Laboratory under US Department of Energy Contract No. DE-AC02-05CH11231. F.W. also acknowledges support from a David and Lucile Packard fellowship. S.T. acknowledges support from NSF CAREER award DMR 1552220. Growth of hexagonal boron nitride crystals was supported by the Elemental Strategy Initiative conducted by the MEXT, Japan and a Grant-in-Aid for Scientific Research on Innovative Areas 'Science of Atomic Layers' from JSPS.

Author contributions

F.W., J.K. and C.J. conceived the research. C.J. and J.K. carried out optical measurements. C.J. and F.W. performed theoretical analysis. J.K., C.J., J.S., Z.S. and M.K. fabricated gate-tunable van der Waals heterostructures. B.C., X.F. and S.T. grew WSe_2 crystals. K.W. and T.T. grew hBN crystals. All authors discussed the results and wrote the manuscript.

Additional information

Supplementary information is available in the online version of the paper. Reprints and permissions information is available online at www.nature.com/reprints. Correspondence and requests for materials should be addressed to F.W.

Competing financial interests

The authors declare no competing financial interests.

© 2016 Macmillan Publishers Limited, part of Springer Nature. All rights reserved.

Methods

Raman features from interlayer electron–phonon coupling are most prominent in the van der Waals heterostructures of WSe_2 encapsulated in hexagonal hBN, which are prepared with a polyethylene terephthalate (PET) stamp by a dry transfer method[32]. Monolayer WSe_2 and ∼10 nm thick hBN flakes are first exfoliated onto silicon substrates with a 90 nm oxide layer. We use the PET stamp to pick up the hBN flake and monolayer WSe_2 in sequence with accurate alignment based on an optical microscope. The PET stamp with the hBN/WSe_2 heterostructure is then stamped onto another hBN flake to form an encapsulated WSe_2 monolayer. Polymer and samples are heated to 60 °C for the pick-up and 130 °C for the stamp process. Finally, we dissolve the PET in dichloromethane for 12 h at room temperature. For the gate dependence study, we purposely picked up a WSe_2 monolayer larger than the top hBN flake to have an electrical contact on the exposed area outside the hBN encapsulation.

Data availability. The data that support the plots within this paper and other findings of this study are available from the corresponding author upon reasonable request.

References

32. Wang, L. *et al*. One-dimensional electrical contact to a two-dimensional material. *Science* **342,** 614–617 (2013).

© 2016 Macmillan Publishers Limited, part of Springer Nature. All rights reserved.